



On the Sound Speed in Neutron Stars

Sinan Altiparmak¹, Christian Ecker¹, and Luciano Rezzolla^{1,2,3}¹Institut für Theoretische Physik, Goethe Universität, Max-von-Laue-Str. 1, D-60438 Frankfurt am Main, Germany; ecker@itp.uni-frankfurt.de²School of Mathematics, Trinity College, Dublin 2, Ireland³Frankfurt Institute for Advanced Studies, Ruth-Moufang-Str. 1, D-60438 Frankfurt am Main, Germany

Received 2022 July 28; revised 2022 August 25; accepted 2022 October 18; published 2022 November 10

Abstract

Determining the sound speed c_s in compact stars is an important open question with numerous implications on the behavior of matter at large densities and hence on gravitational-wave emission from neutron stars. To this scope, we construct more than 10^7 equations of state (EOSs) with continuous sound speed and build more than 10^8 nonrotating stellar models consistent not only with nuclear theory and perturbative QCD, but also with astronomical observations. In this way, we find that EOSs with subconformal sound speeds, i.e., with $c_s^2 < 1/3$ within the stars, are possible in principle but very unlikely in practice, being only 0.03% of our sample. Hence, it is natural to expect that $c_s^2 > 1/3$ somewhere in the stellar interior. Using our large sample, we obtain estimates at 95% credibility of neutron-star radii for representative stars with 1.4 and 2.0 solar masses, $R_{1.4} = 12.42^{+0.52}_{-0.99}$ km, $R_{2.0} = 12.12^{+1.11}_{-1.23}$ km, and for the binary tidal deformability of the GW170817 event, $\tilde{\Lambda}_{1.186} = 485^{+225}_{-211}$. Interestingly, our lower bounds on the radii are in very good agreement with the prediction derived from very different arguments, namely, the threshold mass. Finally, we provide simple analytic expressions to determine the minimum and maximum values of $\tilde{\Lambda}$ as a function of the chirp mass.

Unified Astronomy Thesaurus concepts: Gravitation (661); Nuclear astrophysics (1129); Fundamental parameters of stars (555); Stellar interiors (1606); Neutron stars (1108); Neutron star cores (1107); Nuclear physics (2077)

1. Introduction

Gravity compresses matter in the core of a neutron star to densities a few times larger than the saturation (number) density of atomic nuclei $n_0 := 0.16 \text{ fm}^{-3}$. A quantity that describes the stiffness of matter, a property required to prevent a static neutron star from collapsing to a black hole, is the sound speed

$$c_s^2 := \left(\frac{\partial p}{\partial e} \right)_s, \quad (1)$$

where the pressure p and the energy density e are related by the equation of state (EOS) and the derivative is considered at constant specific entropy s . Calculating the EOS of cold matter at the densities reached in the innermost part of a neutron star is still an open problem. Causality and thermodynamic stability imply $0 \leq c_s^2 \leq 1$, which poses the minimal requirement the EOS has to satisfy. Beyond this basic causality requirement, there are theoretical constraints on the EOS, and therefore on the sound speed, available in two different regimes. In particular, at small densities, i.e., $n \lesssim n_0$, the EOS is well described by effective field theory models (Hebeler et al. 2013; Gandolfi et al. 2019; Keller et al. 2021) and the corresponding sound speed is found to be small $c_s^2 \ll 1$. At larger densities—much higher than those realized inside neutron stars, i.e., $n \gg n_0$ —matter is in a state of deconfined quarks and gluons and the EOS of quantum chromodynamics (QCD) becomes accessible to perturbation theory. Because conformal symmetry of QCD is restored at asymptotically large densities, the sound

speed approaches the value in conformal field theory and realized in ultrarelativistic fluids $c_s^2 = 1/3$ from below. Between these two limits, the EOS is not accessible by first-principle techniques and the sound speed is essentially unknown.

Given this considerable uncertainty, at least three different scenarios are possible for the sound speed as a function of density: (i) monotonic and subconformal: $c_s^2 < 1/3$; (ii) nonmonotonic and subconformal: $c_s^2 < 1/3$; (iii) nonmonotonic and subluminal: $c_s^2 \leq 1$. Clearly, scenarios (ii) and (iii) imply at least one local maximum in the sound speed, which in (iii) can reach values larger than $1/3$. That the sound speed is small at low densities and approaches the conformal value at asymptotically large densities from below could be seen as evidence for an universal bound $c_s^2 < 1/3$, thus favoring scenario (i) and (ii). However, as already pointed out by Bedaque & Steiner (2015), this bound is in tension with the most-massive neutron stars observed and by a number of counter examples in QCD at large isospin density (Carignano et al. 2017), two-color QCD (Hands et al. 2006), quarkyonic matter (McLerran & Reddy 2019; Duarte et al. 2021; Margueron et al. 2021), models for high-density QCD (Leonhardt et al. 2020; Braun & Schallmo 2022; Pal et al. 2022), and models based on the gauge/gravity duality (Ecker et al. 2017; Demircik et al. 2022; Kovensky et al. 2022). All of these examples favor scenario (iii). Finally, astrophysical measurements of neutron-star masses $M \gtrsim 2 M_\odot$ (Antoniadis et al. 2013; Cromartie et al. 2019; Fonseca et al. 2021) and theoretical predictions on the maximum (gravitational) mass (Margalit & Metzger 2017; Rezzolla et al. 2018; Ruiz et al. 2018; Shibata et al. 2019; Nathanail et al. 2021) suggest stiff EOSs with $c_s^2 \gtrsim 1/3$ at densities $\gtrsim n_0$, again selecting the scenario (iii) as the most likely (see also Moustakidis et al. 2017; Kanakis-Pegios et al. 2020, who study upper limits on c_s^2

by extending various EOSs with a maximally stiff parameterization at high densities).

In this Letter, we investigate which of these scenarios is the most natural by exploiting an agnostic approach in which we build a very large variety of EOSs that satisfies constraints from particle theory and astronomical observations. More specifically, we construct the EOSs using the sound-speed parameterization introduced by Annala et al. (2020), which avoids discontinuities in the sound speed as those appearing in a piecewise polytropic parameterization Most et al. (2018b) (see also alternatives that guarantee smoothness, like the spectral approach of Lindblom & Indik 2012, or the Gaussian parameterizations by Greif et al. 2019). We then compute the probability density function (PDF) of the sound speed as derived from the 1.7×10^6 EOSs that satisfy all the constraints. The behavior of the PDF then provides a very effective manner to determine which of the scenarios mentioned above is the most natural given (micro)physical and (macro)astrophysical constraints.

2. Methods

The EOSs we construct are a patchwork of several different components (see the Appendix for a schematic diagram). First, at densities $n < 0.5 n_0$ we use a tabulated version of the Baym–Pethick–Sutherland (BPS) model (Baym et al. 1971). Second, in the range $0.5 n_0 < n < 1.1 n_0$ we construct monotropes of the form $p(n) = K n^\Gamma$, where K is fixed by matching to the BPS EOS and sample uniformly $\Gamma \in [1.77, 3.23]$ to ensure that the pressure remains entirely between the soft and stiff EOSs of Hebeler et al. (2013). Third, between $1.1 n_0 < n \lesssim 40 n_0$ we use the parameterization method introduced by Annala et al. (2020), which uses the sound speed as function of the chemical potential μ as a starting point to construct thermodynamic quantities. In this way, the number density can be expressed as

$$n(\mu) = n_1 \exp\left(\int_{\mu_1}^{\mu} \frac{d\mu'}{\mu' c_s^2(\mu')}\right), \quad (2)$$

where $n_1 = 1.1 n_0$ and $\mu_1 = \mu(n_1)$ is fixed by the corresponding chemical potential of the monotrope. Integrating Equation (2) then gives the pressure

$$p(\mu) = p_1 + \int_{\mu_1}^{\mu} d\mu' n(\mu'), \quad (3)$$

where the integration constant p_1 is fixed by the pressure of the monotrope at $n = n_1$. We integrate Equation (3) numerically, using a fixed number N (3, 4, 5, 7) of piecewise linear segments for the sound speed of the following form

$$c_s^2(\mu) = \frac{(\mu_{i+1} - \mu)c_{s,i}^2 + (\mu - \mu_i)c_{s,i+1}^2}{\mu_{i+1} - \mu_i}, \quad (4)$$

where μ_i and $c_{s,i}^2$ are parameters of the i th segment in the range $\mu_i \leq \mu \leq \mu_{i+1}$. The values of $c_{s,1}^2$ and μ_1 are fixed by the monotrope. Note that we do not sample $c_{s,i}^2 \in [0, 1]$, since this would lead to a statistical suppression of the subconformal EOSs with large number of segments. Rather, for each EOS, we first choose randomly the maximum sound speed $c_{s,\max}^2 \in [0, 1]$ and then uniformly sample the remaining free coefficients $\mu_i \in [\mu_1, \mu_{N+1}]$ and $c_{s,i}^2 \in [0, c_{s,\max}^2]$ in their respective domains.

As the final step in our procedure, we keep solutions whose pressure, density, and sound speed at $\mu_{N+1} = 2.6$ GeV are consistent with the parameterized perturbative QCD result for cold quark matter in beta equilibrium (Fraga et al. 2014)

$$p_{\text{QCD}}(\mu, X) := \frac{\mu^4}{108\pi^2} \left(c_1 - \frac{d_1 X^{-\nu_1}}{\mu/\text{GeV} - d_2 X^{-\nu_2}} \right), \quad (5)$$

where $c_1 = 0.9008$, $d_1 = 0.5034$, $d_2 = 1.452$, $\nu_1 = 0.3553$, $\nu_2 = 0.9101$, and the renormalization scale parameter $X \in [1, 4]$. All of the results presented in the main text refer to 1.5×10^7 EOSs constructed with $N = 7$ segments (see the Appendix for details).

To impose the observational constraints, we compute the mass–radius relation for each EOS by numerically solving the Tolman–Oppenheimer–Volkoff (TOV) equations; since we construct $\simeq 10^2$ TOV solutions for each EOS, we can count on a statistics of $\simeq 1.2 \times 10^8$ nonrotating stellar models. We impose the mass measurements of J0348+0432 (Antoniadis et al. 2013; $M = 2.01 \pm 0.04 M_\odot$) and of J0740+6620 (Cromartie et al. 2019; Fonseca et al. 2021; $M = 2.08 \pm 0.07 M_\odot$) by rejecting EOSs that have a maximum mass $M_{\text{TOV}} < 2.0 M_\odot$. In addition, we impose the radius measurements by NICER of J0740+6620 (Miller et al. 2021; Riley et al. 2021) and of J0030+0451 (Riley et al. 2019; Miller et al. 2019) by rejecting EOSs with $R < 10.75$ km at $M = 2.0 M_\odot$ and $R < 10.8$ km at $M = 1.1 M_\odot$, respectively (see Figure 6 in the Appendix). Finally, we exploit the detection of GW171817 by LIGO/Virgo to set an upper bound on the binary tidal deformability $\tilde{\Lambda} < 720$ (low-spin priors; The LIGO Scientific Collaboration et al. 2019). Denoting respectively with M_i , R_i , and Λ_i the masses, radii, and tidal deformabilities of the binary components, where $\Lambda_i = \frac{2}{3} k_2 (R_i/M_i)^5$, $i = 1, 2$, and k_2 is the second tidal Love number, we compute the binary tidal deformability as

$$\tilde{\Lambda} := \frac{16 (12M_2 + M_1)M_1^4 \Lambda_1 + (12M_1 + M_2)M_2^4 \Lambda_2}{13 (M_1 + M_2)^5}. \quad (6)$$

For any choice of $M_{1,2}$ and $R_{1,2}$, we then reject those EOSs with $\tilde{\Lambda} > 720$ for a chirp mass $\mathcal{M}_{\text{chirp}} := (M_1 M_2)^{3/5} (M_1 + M_2)^{-1/5} = 1.186 M_\odot$ and $q := M_2/M_1 > 0.73$ as required for consistency with LIGO/Virgo data for GW170817 (Abbott et al. 2018).

3. Results

In order to build the various PDFs, we discretize the corresponding two-dimensional space of solutions (e.g., in the (M, R) space) in 700×700 equally spaced cells (either linearly or logarithmically), count the number of curves that cross a certain cell, and normalize the result by the maximum count on the whole grid. Because the normalization is made in two dimensions, slices along a fixed direction do not yield normalized distributions.

Figure 1 shows the PDF of c_s^2 as a function of the energy density, with the purple region marking the 95% range of maximum central energy densities, that is, the central energy density reached by any EOS by the star with the maximum mass M_{TOV} . Stated differently, the right edge of the purple region (vertical purple line) marks our estimate for the largest possible energy density encountered in a neutron star; in our

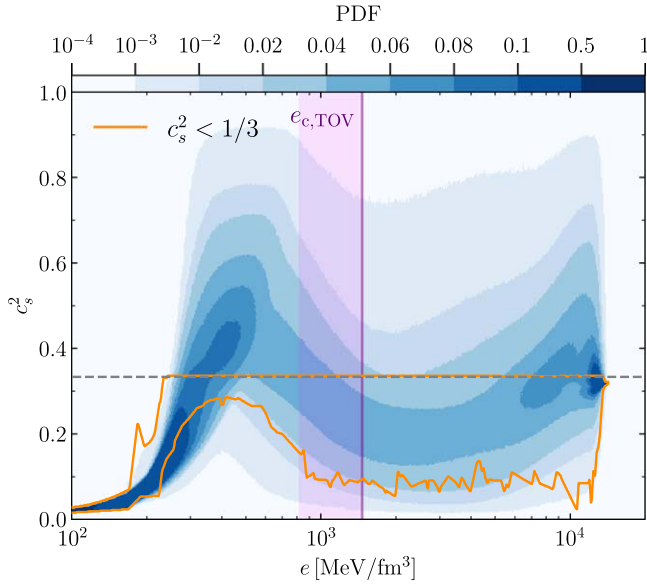


Figure 1. PDF of the sound speed squared as function of the energy density. The purple region marks the 95% interval of maximum central energy densities, so that the vertical purple line represents an estimate for the largest possible energy density in a neutron star. The orange contour marks the region containing EOSs with $c_s^2 < 1/3$.

sample, we obtain the median $e_{c,\text{TOV}} = 1064^{+399}_{-244}$ MeV/fm³ at 95% confidence.

Note that the PDF shows a steep increase to $c_s^2 \gtrsim 1/3$ for $e \lesssim 500$ MeV/fm³, thus signalling a significant stiffening of the EOS at these densities and a subsequent decrease of the sound speed for larger energy densities. As a result, the PDF illustrates how a nonmonotonic behavior is most natural for the sound speed, hence how the physical and observational constraints favor scenario (iii). Models for quarkyonic matter (see, e.g., McLerran & Reddy 2019) typically show a peak at low densities similar to the one in our PDF (Hippert et al. 2021).

The orange line in Figure 1 marks the region of the EOSs that are subconformal, i.e., with $c_s^2 < 1/3$, at all densities (the horizontal dashed line that marks $c_s^2 = 1/3$). Note that around 500 MeV/fm³, the orange contour spans a very thin region, indicating that at these energy densities the subconformal EOSs have an obvious upper bound $c_s^2 < 1/3$, but also a less-obvious lower bound $c_s^2 \gtrsim 0.2$. This is an important feature that explains why these EOSs are so difficult to produce. Indeed, as revealed by the color map, the number of EOSs that fall in this region is very small and amounts to only $\simeq 5 \times 10^{-5}$ of the total. The fraction of subconformal EOSs increases slightly if we restrict the range of densities to those that are admissible for neutron-star interiors, becoming $\simeq 3 \times 10^{-4}$ of the total. The reason for this increase is that many of the EOSs that are subconformal for $e \lesssim 300$ MeV/fm³, tend to stiffen at larger energy densities, thus becoming superconformal.

The color map of the PDF in Figure 1 also reveals the presence of a second peak at large energy densities, close to where the perturbative QCD boundary conditions are imposed and reflects artifacts of the parameterization method, which allows for large variations in the sound speed at very high energy densities, where c_s^2 is expected to be close to the asymptotic value 1/3. Fortunately, the energy densities where this second peak appears are far from those expected in the interior of neutrons stars. It is also possible to reduce the extent

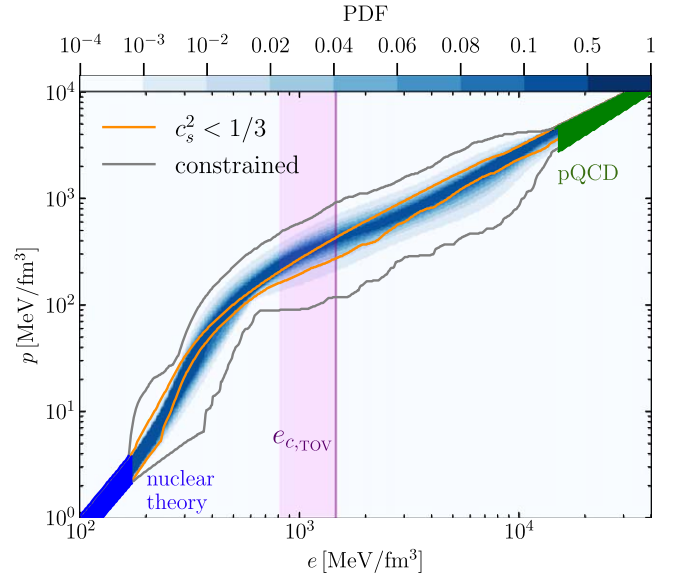


Figure 2. PDF of the pressure as function of the energy density. The blue and green regions mark the uncertainties in pressure in nuclear theory (Hebeler et al. 2013) and perturbative QCD (Fraga et al. 2014), respectively. The gray contour encloses all EOSs satisfying the astronomical constraints, while the purple regions and the orange contour are the same as in Figure 1.

of this second peak by imposing a criterion that filters out EOSs whose sound speeds vary strongly on small scales as done by Annala et al. (2020). However, given the very poor knowledge of the behavior of the sound speed at these regimes, we prefer to report the unfiltered results. What matters here is that, when imposed, the filtering has no significant impact on the PDF at the energy densities that are relevant for stellar interiors (see the Appendix for a discussion).

Figure 2 shows the corresponding PDF of the pressure as a function of the energy density with the same conventions as in Figure 1. In addition, we indicate with a gray line the outer envelope of all constraint-satisfying solutions, which is very similar to the one found by Annala et al. (2020). However, an important difference with respect to Annala et al. (2020), where no information on the distribution is offered, is that the PDF reveals that the large majority of EOSs accumulates in a band that is much narrower than the allowed gray region. Interestingly, at almost all energy densities, the pressure is either inside or close to the subconformal region, except around $e \approx 500$ MeV/fm³. This is an important result as it reveals that it is very hard to deduce the poor likelihood of subconformal EOSs when looking at the behavior of the pressure only.

Figure 3 shows the PDF of the masses as a function of the stellar radii. The outer edges of the distribution show $M_{\text{TOV}} \lesssim 3 M_{\odot}$ and an approximate lower limit for the minimum radius of $R \gtrsim 10.5$ km. This is in remarkably good agreement with the analytic lower bound $R/\text{km} \gtrsim -0.88(M/M_{\odot})^2 + 2.66(M/M_{\odot}) + 8.91$ derived when using the detection of GW170817 and the estimates on the threshold mass to prompt collapse (Koepfel et al. 2019; Tootle et al. 2021). The orange line marks again the outer envelope spanned by subconformal EOSs, whose maximum mass is $M \approx 2.1 M_{\odot}$, also seen by Annala et al. (2020, 2022). This behavior confirms on rather general grounds the tension between $c_{s,\text{max}}^2 < 1/3$ and the observation of stars with $M \gtrsim 2 M_{\odot}$, already been pointed out (see, e.g., Alford et al. 2015; Bedaque & Steiner 2015; Tews et al. 2018).

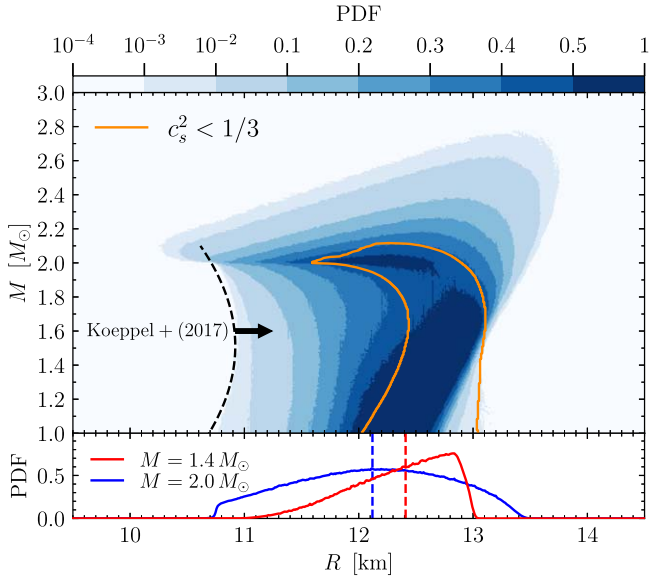


Figure 3. Top: PDF of the mass–radius relation. The orange contour encloses EOSs with subconformal sound speed (see Figure 1). The dashed black line reports the lower bound for the radii as computed from considerations on the threshold mass (Koepfel et al. 2019). Bottom: PDF cuts for stars with mass $M = 1.4 M_{\odot}$ and $M = 2.0 M_{\odot}$; the dashed vertical lines mark the median of the distributions.

In the bottom panel of Figure 3 we report slices of the PDF for two selected masses, namely, 1.4 and $2.0 M_{\odot}$. The median values (dashed lines) and the 95% confidence levels allow us to estimate the corresponding radii as $R_{1.4} = 12.42^{+0.52}_{-0.99}$ km and $R_{2.0} = 12.11^{+1.11}_{-1.23}$ km, respectively. The significant skew in the distribution for $M = 1.4 M_{\odot}$ is due to the tidal-deformability constraint that penalizes large radii. Despite the different method, our estimate for the median of $R_{1.4}$ is in good agreement with the piecewise polytropic estimates of Most et al. (2018a) ($12.00 < R_{1.4} < 13.45$ km) and slightly larger, but well within the error bars of the estimates by Huth et al. (2021; see also Abbott et al. 2018; Radice & Dai 2019; Capano et al. 2020; Dietrich et al. 2020; Biswas et al. 2021, for similar estimates).

Interestingly, we find that none of our constraint-satisfying EOSs have monotonic sound speeds, as it is required by scenario (i). In order to check if the scenario (i) is just unlikely or indeed inconsistent with the constraints, we construct 1.5×10^7 EOSs with monotonic sound speed, hence sampling the sound speed in $c_s^2 \in [0, 1/3]$, without imposing a lower bound on M_{TOV} . We then find that these EOSs are only able to support a maximal mass $M_{\text{TOV}} < 1.99 M_{\odot}$ and are therefore excluded by a two-solar-mass bound (see the Appendix for the PDF of this constraint-violating subset).

We conclude our discussion on the statistical properties of our EOSs with what arguably is one of the most important results of this work. More specifically, we report in Figure 4 the PDF of the binary deformability shown as a function of the chirp mass. In essence, for any EOS in our sample, we randomly collect 100 pairs of $M_{1,2}$, $\Lambda_{1,2}$, out of which we compute $\mathcal{M}_{\text{chirp}}$ and $\tilde{\Lambda}$. The results are then binned and color coded as in the other PDFs. We find this is a particularly important figure as it relates a quantity that is directly measurable from gravitational-wave observations, $\mathcal{M}_{\text{chirp}}$, with a quantity that contains precious information on the micro-physics $\tilde{\Lambda}$. In this way, we find that the binary tidal

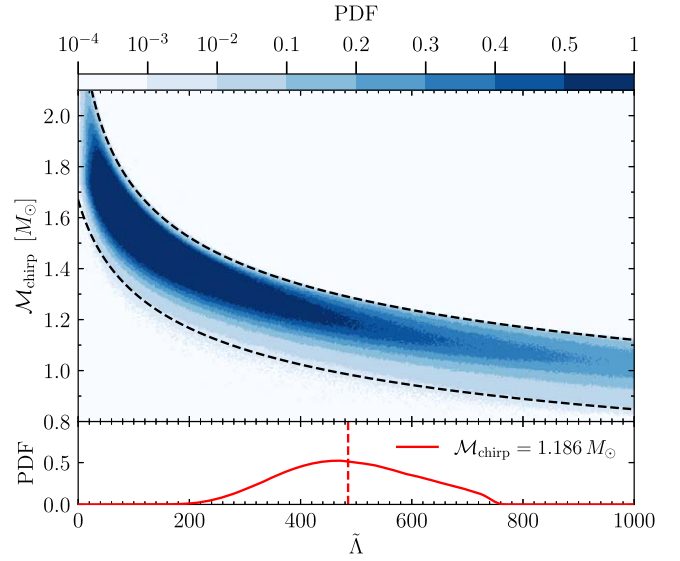


Figure 4. Top: PDF of the chirp mass as a function of the binary tidal deformability. Shown as black dashed lines are analytic fits for the minimum and maximum values of $\tilde{\Lambda}$ for a given chirp mass. Bottom: PDF cut for a binary with the same chirp mass as in GW170817, $\mathcal{M}_{\text{chirp}} = 1.186 M_{\odot}$; the red dashed vertical line marks the median.

deformability of a GW170817-like event is constrained to be $\tilde{\Lambda}_{1.186} = 483^{+224}_{-210}$, at a 95% confidence level. The lower bound is a prediction while the upper bound effectively reflects the constraint imposed on $\tilde{\Lambda}$. Furthermore, we have fitted the 99% confidence contours of the PDF with simple power laws (dashed black lines) to obtain analytic estimates for the minimum (maximum) value of $\tilde{\Lambda}$ as function of the chirp mass

$$\tilde{\Lambda}_{\text{min(max)}} = a + b \mathcal{M}_{\text{chirp}}^c, \quad (7)$$

where $a = -50(-20)$, $b = 500(1800)$, and $c = -4.5(-5.0)$. The relevance of Equation (7) is that, once a merging neutron-star binary is detected and its chirp mass is measured accurately, it is straightforward to use Equation (7) to readily obtain a lower and an upper bound on the binary tidal deformability of the system. This has not been possible so far, where only upper limits have been set (Abbott et al. 2018).

Finally, to provide a graphical representation of our statistics, we show in Figure 5 the relative weight of the various sets into which our total sample of EOSs can be decomposed, either when subject to the observational constraints (dark blue) or when not (light blue). Note that the heights of the light-blue bars in Figure 5 for scenarios (i) (fourth bar) and (iii) (first bar) are not the same. In other words, the unconstrained samples of these scenarios are not equally populated. This is simply because we sample the sound speed uniformly, so that the EOSs in which all of the values of c_s^2 have to fall below $1/3$, as required for scenario (i), are statistically suppressed when compared to the generic scenario (iii), where c_s^2 can assume values in the full range $[0, 1]$. What matters, however, is the relative difference in the constrained/unconstrained samples (see stellar markers), which is 1 order of magnitude smaller for scenario (i) than for scenario (iii). This means that (iii) is statistically preferred over (i) by the observational data. Furthermore, we note that in our full set we do not find any EOS with monotonic c_s^2 at all densities that satisfies the observational constraints.

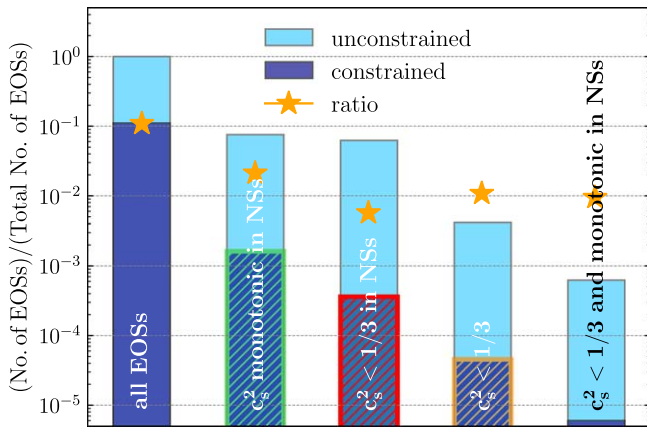


Figure 5. Schematic representation of the various sets into which our total sample of EOSs can be decomposed, either when subject to the observational constraints (dark blue) or when not (light blue). The ratio between the two samples is shown with a stellar marker, while the hatched color coding reflects that used in Figure 1 and in the Appendix.

4. Conclusion

We have constructed a large number of viable EOSs and studied the statistical distributions of the corresponding sound speed, mass–radius relation, and binary tidal deformability. We found that a steep rise in the sound speed and a peak $c_s^2 > 1/3$ is statistically preferred and that EOSs with subconformal sound speeds, i.e., $c_s^2 \leq 1/3$, are possible within the stars, but also that they are unlikely, although in principle possible, being only 0.03% of our sample. Hence, it is natural to expect that $c_s^2 > 1/3$ somewhere inside the neutron stars. Furthermore, imposing subconformality already at the level of the sampling has allowed us to resolve the range of these EOSs more accurately and identify a lower bound for the sound speed $c_s^2 \gtrsim 0.2$ around $e \approx 590 \text{ MeV}/\text{fm}^3$. Interestingly, we were not able to find solutions with monotonic sound speed. Exploiting the statistical robustness of our large sample, we have obtained estimates at 95% credibility of neutron-star radii for representative stars with masses of 1.4 and 2.0 solar masses, namely, $R_{1.4} = 12.42^{+0.52}_{-0.99} \text{ km}$, $R_{2.0} = 12.12^{+1.11}_{-1.23} \text{ km}$, and for the binary tidal deformability of the GW170817, $\tilde{\Lambda}_{1.186} = 485^{+225}_{-211}$.

Remarkably, the very agnostic predictions on the mass–radius relations emerging from our statistics matches well the analytic predictions on the minimum stellar radius coming from very different arguments, namely the threshold mass to gravitational collapse. New radius and mass measurements, as well as gravitational-wave detections of binary neutron-star mergers will allow us to improve these estimates and narrow down our PDFs further. For example, the discovery of a neutron star with mass larger than $2.1 M_\odot$ would eliminate the possibility of subconformal EOSs entirely. Future work will consider improved constraints at neutron-star densities from perturbative QCD such as those recently suggested by Komoltsev & Kurkela (2022). In addition, alternative approaches to the construction of the EOSs (e.g., piecewise polytropes, Most et al. 2018b; or spectral parameterization, Lindblom & Indik 2012) will help determine a potential bias introduced by our method, which is, however, expected to be much smaller than the observational uncertainties.

Note: After the completion of this work, a new mass measurement of $2.35 \pm 0.17 M_\odot$ has been published for the

pulsar in the binary system PSR J0952-0607 (Romani et al. 2022). This new mass bound has no impact on the main results and conclusions presented here. While a detailed discussion is beyond the scope of this paper, the impact of very large maximum masses on the internal properties of neutron stars has instead been analyzed (Ecker & Rezzolla 2022).

We thank R. Duque, T. Gorda, J. Jiang, and A. Vuorinen for valuable discussions and comments on the manuscript, as well as A. Cruz-Osorio and K. Topolski for help with the visualizations. Partial funding comes from the State of Hesse within the Research Cluster ELEMENTS (Project ID 500/10.006), by the ERC Advanced Grant “JETSET: Launching, propagation and emission of relativistic jets from binary mergers and across mass scales” (Grant No. 884631). C. E. acknowledges support by the Deutsche Forschungsgemeinschaft (DFG, German Research Foundation) through the CRC-TR 211 “Strong-interaction matter under extreme conditions”–project number 315477589–TRR 211.

Appendix Details about EOS Construction

The material presented here is meant to provide additional information on some of the details of our calculations and on their robustness.

We start by showing in Figure 6 some illustrative examples of our method for the construction of the EOSs. For simplicity, we concentrate on three representative examples referring to a generic EOS (i.e., an EOS with no specific behavior of the sound speed; red solid line), a subconformal EOS (i.e., an EOS with $c_s^2 < 1/3$; blue solid line), and monotonic sound speed inside neutron stars (i.e., an EOS with monotonic c_s^2 for $e \lesssim e_{c,\text{TOV}} \approx 1.3 \text{ GeV fm}^{-3}$ in this case; green solid line). More specifically, the plot on the left shows the sound speed as function of the energy density; note that the curves are continuous but with discontinuous derivatives and that the kinks in the curves mark the matching points of the various segment used to construct the EOSs. The middle panel shows the corresponding EOSs, together with the BPS EOS (Baym et al. 1971) (cyan solid line) that we use at low densities. The blue and green bands are the uncertainties from nuclear theory (Hebeler et al. 2013) and perturbative QCD (Fraga et al. 2014), respectively. We also show in gray the outer envelope of all constraint-satisfying EOSs. Finally, the right panel shows the corresponding mass–radius curves, together with the outer envelope and various observational constraints (Antoniadis et al. 2013; Cromartie et al. 2019; Fonseca et al. 2021; Miller et al. 2021; Riley et al. 2021) we impose. Note that the gray contour reproduces the hump at large radii around $M \approx 1.2 M_\odot$, also seen by Annala et al. (2020), and which was associated to dynamically unstable solutions by Jiménez & Fraga (2021). Comparing this part of the contour to Figure 3 in the main text clearly shows that the solutions in this region are possible but very unlikely.

Figure 1 of the main text shows the PDF of c_s^2 as a function of the energy density and a discretized color map. Note that the steep increase to $c_s^2 \gtrsim 1/3$ for $e \lesssim 500 \text{ MeV}/\text{fm}^3$, thus signalling a significant stiffening of the EOS at these densities and a subsequent decrease of the sound speed for larger energy densities. As a visual aid on how this steep increase is produced, Figure 7 is the same as Figure 1 in the main text, but

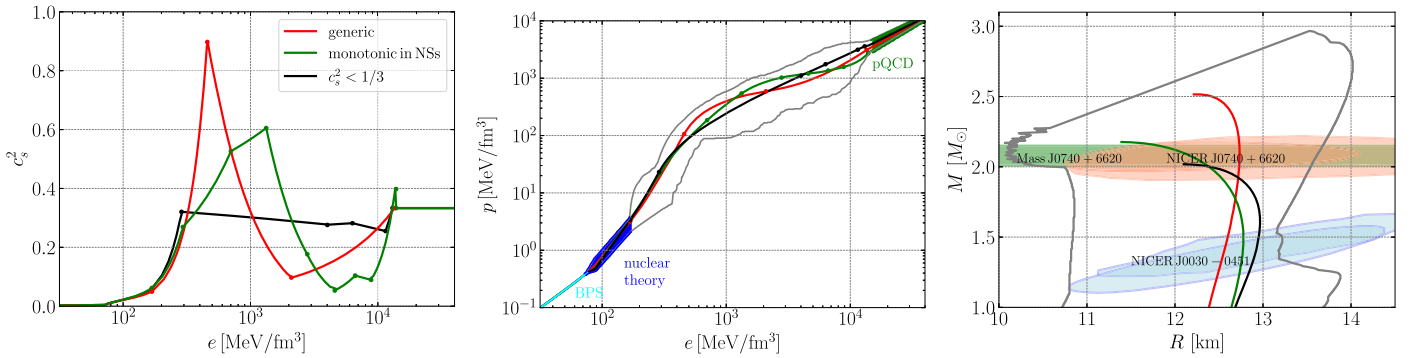


Figure 6. Representative examples referring to a generic EOS (red solid line), a subconformal EOS (blue solid line), and monotonic sound speed inside neutron stars (green solid line). The left plot shows the sound speed as function of the energy density, with the kinks marking the matching points of the various segment used to construct the EOSs. The middle panel shows the corresponding EOSs, together with the BPS EOS (Baym et al. 1971; cyan solid line) that we use at low densities. The blue and green bands are the uncertainties from nuclear theory (Hebeler et al. 2013) and perturbative QCD (Fraga et al. 2014), respectively. Shown in gray is the outer envelope of all constraint-satisfying EOSs. The right panel reports the corresponding mass–radius curves, together with the outer envelope and various observational constraints.

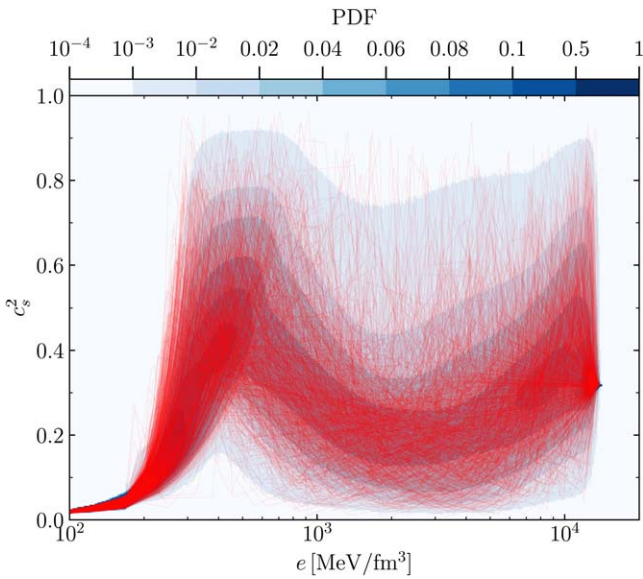


Figure 7. The same as Figure 1 in the main text, but with the overlay of the sound-speed curves relative to 1000 different EOSs.

with the overlay of the sound-speed curves relative to 1000 different EOSs.

We next consider the impact that the number of segments employed in the construction of the piecewise linear segments for the calculation of the sound speed. As pointed out by Annala et al. (2020), constructing EOSs from piecewise linear segments for the sound speeds can lead to rather extreme EOSs, that is, EOSs having rapidly changing material properties, especially close to where the boundary conditions are imposed. We also observe this effect in our calculation and find it to be enhanced when using a large number of segments. In principle, it is possible to introduce a criterion that discards such solutions with strongly varying sound speed. For example, Annala et al. (2020) demanded that the energy densities at two successive inflection points do not have an excessive relative variation, i.e., $(e_i - e_{i+1})/e_i > \Delta \ln e$ with $\Delta \ln e = 0.5$. In this way, models with steep gradients on small energy scales are filtered out. Here, however, and as mentioned in the main text, we have decided not to apply such a filter but provide evidence in this section that the first peak in the sound speed is a robust feature that is independent of the number of segments and filtering.

A sufficiently large number of segments is important to avoid a too coarse description of the sound speed and related artifacts that we discuss further below. We note that the setup just described is able to approximate phase transitions very closely. However, obtaining a “perfect” first-order phase transition requires that two consecutive draws for the sound speed are exactly zero. Since we do not explicitly demand that this happens, perfect first-order phase transitions are very unlikely in practice, but our results include a number of cases with very low sound speed at two neighboring matching points. On the one hand, choosing N to be small could lead to EOSs that are rather crude and possibly suffer from intrinsic biases. On the other hand, if N is very large, the whole construction can be excessively expensive from a computational point of view. Hence, an optimal choice needs to be found for N . In Figure 8 we compare the PDFs for different values of the number of segments with and without filtering. Choosing a low number of segments (e.g., $N=3, 4$) has the effect of influencing the distribution of the sound speed mostly at intermediate and high densities close to the perturbative QCD boundary conditions. This is shown in the first two panels on the left of Figure 8, which refer to $N=3, 4$, respectively; the third panel from the left refers instead to $N=5$ and clearly indicate that a sufficiently large number of segments is necessary to avoid artifacts at large energy densities. When comparing the PDF for $N=5$ with that obtained in Figure 1 of the main text, where $N=7$, indicates that the latter is already a sufficiently large number of segments; indeed, experiments carried out on a limited set of EOSs with $N=9$ has shown that the differences in the PDFs are very small. Overall, the first three panels of the figure show that the steep increase of the distribution beyond $c_s^2 \simeq 1/3$ at small energy densities is a robust result that is independent of the number of segments and filtering. Finally, note that the rightmost panel in Figure 8 refers to a PDF for $N=5$ in which the filtering on the energy-density gradient is applied. Note how the filtering does modify the behavior of the PDF at very large energy densities removing the most extreme EOSs. It remains unclear whether this should be considered as a more realistic PDF.

Having a different number of segments also impacts the PDFs of the pressure as a function of the energy density. This is reported in Figure 9, which shows the outer envelope of constraint-satisfying solutions for different numbers of segments and reported with various gray curves. Note that all

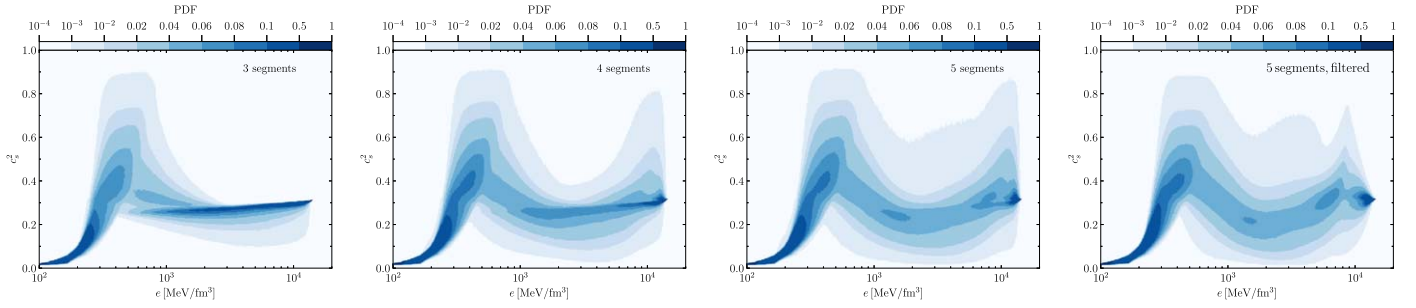


Figure 8. PDFs of the sound speed obtained for different values of the number of segments. More specifically, the first three panels from the left refer to $N = 3, 4, 5$, respectively. They clearly show that the steep increase of the distribution beyond $c_s^2 \simeq 1/3$ at small energy densities is a robust result that is independent of the number of segments and filtering. The rightmost panel refers instead to a PDF for $N = 5$ in which the filtering on the energy-density gradient is applied. Note how the filtering does modify the behavior of the PDF at very large energy densities removing the most extreme EOSs.

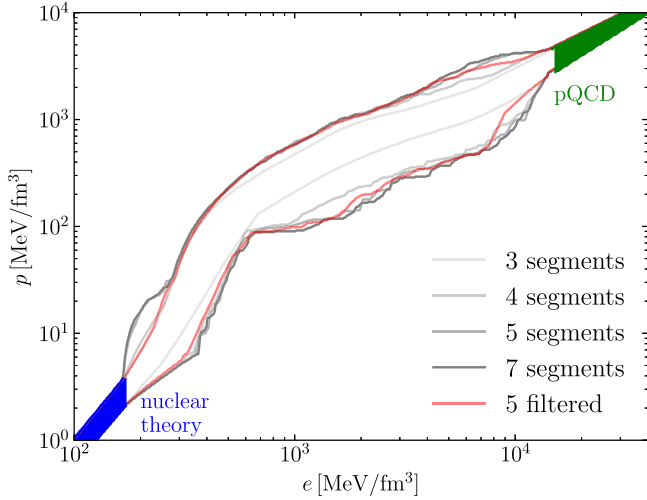


Figure 9. Outermost contours of constraint-satisfying EOSs. Gray curves are obtained from unfiltered sampling with three, four, five, and seven segments; the light-red contour refers to the five-segment EOS after filtering.

PDFs refer to the EOSs that have not been filtered, while the light-red curve is the result for five segments and a filter on the relative energy density $\Delta \ln e = 0.5$. Note that a parameterization with three segments results in a band that is significantly narrower than for larger numbers of segments. However, a comparison with Figure 2, which was done with seven segments, suggests that most of the missed solutions fall inside the sparsely populated region. Increasing the number of segments from three to seven clearly shows that already five segments lead to a well-converged result for the outer envelope. Finally, inspecting the light-red curve it is possible to appreciate that the filtering affects mostly the regions close to the boundary conditions at low and very high energy densities, leaving the contours in between essentially unchanged.

We should note that the position of the peak in the sound speed at neutron-star densities is most probably related to the boundary conditions set at high densities. Ideally, it would be interesting to study how the properties of the peak in the sound speed varies when different boundary conditions in the pQCD limit are imposed. Doing so is, however, less trivial than it seems. The actual reason for this peak (see also Gorda et al. 2022) is not so much the conformal value of the sound speed, but, rather, the values of the QCD pressure and the fact that they must be approached in a causal manner by our sampled EOS models. In order to relax these boundary condition one

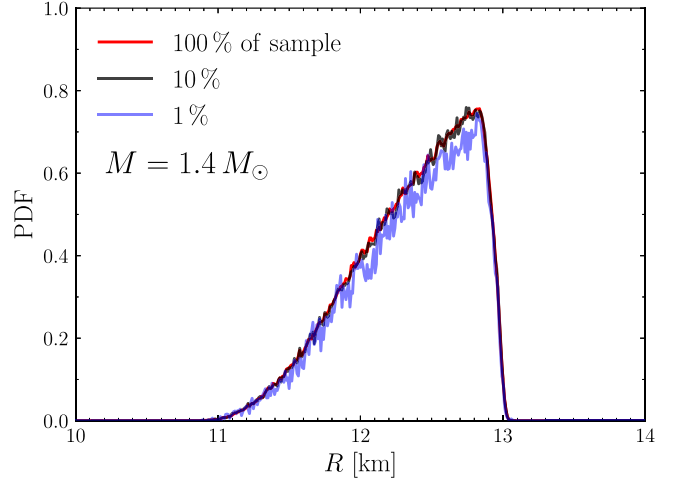


Figure 10. PDF of stellar radii at a fixed mass $M = 1.4 M_\odot$ for different fractions of our sample. Clearly, having a large number of EOSs decreases the size of the fluctuations; however 10% of the sample is already sufficient to obtain robust estimates of the median.

would need to define a new range for the pressure as well as a relation between the pressure and the energy density that leads to the desired value of the sound speed. This is equivalent to formulating an alternative EOS model that would differ from the established perturbative QCD result. If such a self-consistent model were available and was employed in our analysis, it would most likely move the location at which the sound speed has to decrease in order to meet the high-density boundary conditions. Unfortunately, however, this model is not presently available, at least to the best of our knowledge; hence, a purely ad hoc change in the high-density regime may lead to physically inconsistent results.

Another aspect of our analysis that is worth discussing is the number of EOS that is necessary to use to have a statistically robust description of the PDFs. As mentioned in the main text, we have computed at total of 1.5×10^7 EOSs and we have found that such a large number is sufficient to obtain a variance that is of $\sim 3\%$ at most. This is shown in Figure 10, which reports a cut of the PDF for a reference mass of $M = 1.4 M_\odot$ when considering different fractions of our sample. In particular, the red line provides the section of the PDF when all EOSs are taken into account and corresponds therefore to the red line reported in the bottom part of Figure 3 of the main text. Shown instead with black and blue lines are the cuts when considering only 10% or 1% of the sample, respectively. Note

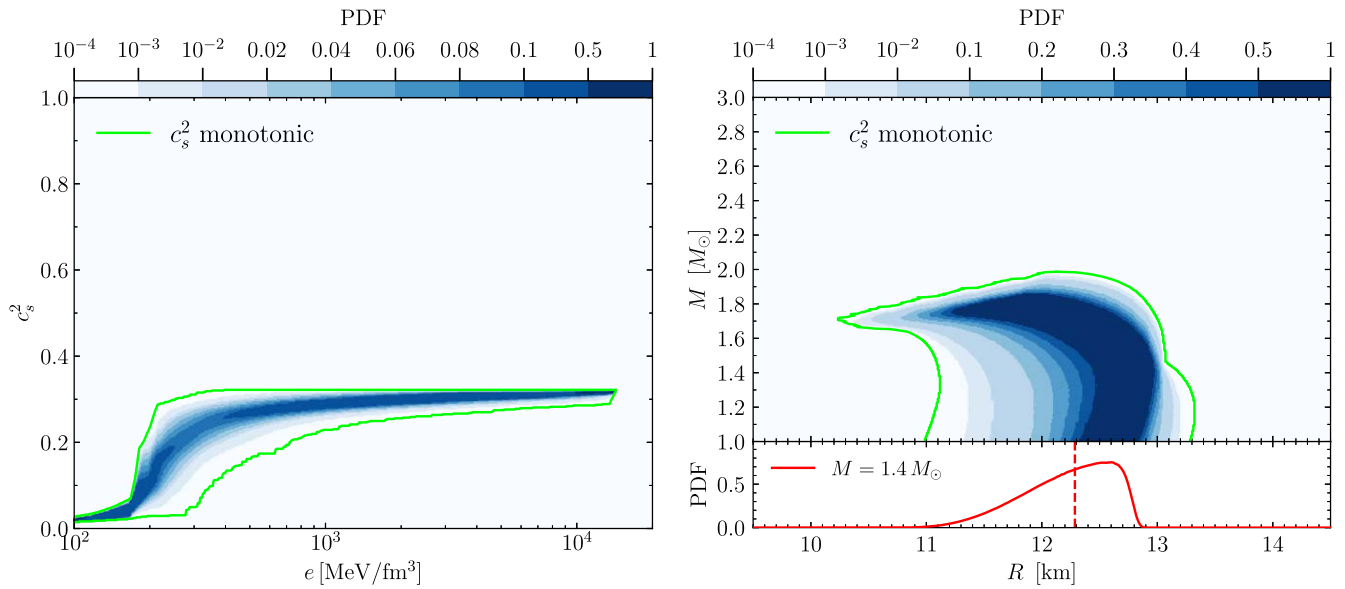


Figure 11. PDF for the sound speed (left panel) and the mass–radius relation (right panel) of monotonic EOSs without observational constraints. Note that no stellar model can be found with mass $M \gtrsim 2 M_{\odot}$.

that having only 10% of the EOSs in the sample is sufficient to obtain robust estimates of the median.

We conclude this Appendix with a discussion focused on the properties of the EOSs that lead to sound speeds that are monotonic. As mentioned in the main text, because these EOSs are rather rare from a statistical point of view, it is convenient to construct our ensemble by sampling the sound speed not across all of its possible values, i.e., $0 \leq c_s^2 \leq 1$, but only in the relevant regime, i.e., $0 \leq c_s^2 \leq 1/3$. In this way, it was possible to produce a separate and rich ensemble of 1.5×10^6 EOSs with sound speed increasing monotonically and for which no observational constraints on the maximum mass were imposed.

These results are summarized in Figure 11, whose two panels show the corresponding PDFs for the sound speed as a function of the energy density (left panel) and of the mass as a function of the stellar radius (right panel). In this respect, they can be compared with Figures 1 and 3 of the main text, where, however, the green contour is now used to mark the entire span of the PDFs. Interestingly and importantly, the PDFs reveal that the largest mass that can be sustained in this case is $M \leq 1.99 M_{\odot}$.

ORCID iDs

Christian Ecker  <https://orcid.org/0000-0002-8669-4300>

Luciano Rezzolla  <https://orcid.org/0000-0002-1330-7103>

References

Abbott, B. P., Abbott, R., Abbott, T. D., et al. 2018, *PhRvL*, **121**, 161101
 Alford, M. G., Burgio, G. F., Han, S., Taranto, G., & Zappalà, D. 2015, *PhRvD*, **92**, 083002
 Annala, E., Gorda, T., Katerini, E., et al. 2022, *PhRvX*, **12**, 011058
 Annala, E., Gorda, T., Kurkela, A., Nättilä, J., & Vuorinen, A. 2020, *NatPh*, **16**, 907
 Antoniadis, J., Freire, P. C. C., Wex, N., et al. 2013, *Sci*, **340**, 6131
 Baym, G., Pethick, C., & Sutherland, P. 1971, *ApJ*, **170**, 299
 Bedaque, P., & Steiner, A. W. 2015, *PhRvL*, **114**, 031103
 Biswas, B., Char, P., Nandi, R., & Bose, S. 2021, *PhRvD*, **103**, 103015
 Braun, J., & Schallmo, B. 2022, *PhRvD*, **106**, 076010
 Capano, C. D., Tews, I., Brown, S. M., et al. 2020, *NatAs*, **4**, 625

Carignano, S., Lepori, L., Mammarella, A., Mannarelli, M., & Pagliaroli, G. 2017, *EPJA*, **53**, 35
 Cromartie, H. T., Fonseca, E., Ransom, S. M., et al. 2019, *NatAs*, **4**, 72
 Demircik, T., Ecker, C., & Järvinen, M. 2022, *PhRvX*, **12**, 041012
 Dietrich, T., Coughlin, M. W., Pang, P. T. H., et al. 2020, *Sci*, **370**, 1450
 Duarte, D. C., Hernandez-Ortiz, S., Jeong, K. S., & McLerran, L. D. 2021, *PhRvD*, **104**, L091901
 Ecker, C., Hoyos, C., Jokela, N., Rodríguez Fernández, D., & Vuorinen, A. 2017, *JHEP*, **11**, 031
 Ecker, C., & Rezzolla, L. 2022, arXiv:2209.08101
 Fonseca, E., Cromartie, H. T., Pennucci, T. T., et al. 2021, *ApJL*, **915**, L12
 Fraga, E. S., Kurkela, A., & Vuorinen, A. 2014, *ApJL*, **781**, L25
 Gandolfi, S., Lippuner, J., Steiner, A. W., et al. 2019, *JPhG*, **46**, 103001
 Gorda, T., Komoltsev, O., & Kurkela, A. 2022, arXiv:2204.11877
 Greif, S. K., Raaijmakers, G., Hebeler, K., Schwenk, A., & Watts, A. L. 2019, *MNRAS*, **485**, 5363
 Hands, S., Kim, S., & Skullerud, J.-I. 2006, *EPJC*, **48**, 193
 Hebeler, K., Lattimer, J. M., Pethick, C. J., & Schwenk, A. 2013, *ApJ*, **773**, 11
 Hippert, M., Fraga, E. S., & Noronha, J. 2021, *PhRvD*, **104**, 034011
 Huth, S., Pang, T. H., Tews, I., et al. 2021, *Natur*, **606**, 276
 Jiménez, J. C., & Fraga, E. S. 2021, *PhRvD*, **104**, 014002
 Kanakis-Pegios, A., Koliogiannis, P. S., & Moustakidis, C. C. 2020, *PhRvC*, **102**, 055801
 Keller, J., Wellenhofer, C., Hebeler, K., & Schwenk, A. 2021, *PhRvC*, **103**, 055806
 Koepfel, S., Bovard, L., & Rezzolla, L. 2019, *ApJL*, **872**, L16
 Komoltsev, O., & Kurkela, A. 2022, *PhRvL*, **128**, 202701
 Kovensky, N., Poole, A., & Schmitt, A. 2022, *PhRvD*, **105**, 034022
 Leonhardt, M., Pospiech, M., Schallmo, B., et al. 2020, *PhRvL*, **125**, 142502
 Lindblom, L., & Indik, N. M. 2012, *PhRvD*, **86**, 084003
 Margalit, B., & Metzger, B. D. 2017, *ApJL*, **850**, L19
 Margueron, J., Hansen, H., Proust, P., & Chanfray, G. 2021, *PhRvC*, **104**, 055803
 McLerran, L., & Reddy, S. 2019, *PhRvL*, **122**, 122701
 Miller, M. C., Lamb, F. K., Dittmann, A. J., et al. 2019, *ApJL*, **887**, L24
 Miller, M. C., Lamb, F. K., Dittmann, A. J., et al. 2021, *ApJL*, **918**, L28
 Most, E. R., Nathanael, A., & Rezzolla, L. 2018a, *ApJ*, **864**, 117
 Most, E. R., Weih, L. R., Rezzolla, L., & Schaffner-Bielich, J. 2018b, *PhRvL*, **120**, 261103
 Moustakidis, C. C., Gaitanos, T., Margaritis, C., & Lalazisis, G. A. 2017, *PhRvC*, **95**, 045801
 Nathanael, A., Most, E. R., & Rezzolla, L. 2021, *ApJL*, **908**, L28
 Pal, S., Kadam, G., & Bhattacharyya, A. 2022, *Nucl. Phys. A*, **1023**, 122464
 Radice, D., & Dai, L. 2019, *EPJA*, **55**, 50
 Rezzolla, L., Most, E. R., & Weih, L. R. 2018, *ApJL*, **852**, L25
 Riley, T. E., Watts, A. L., Bogdanov, S., et al. 2019, *ApJL*, **887**, L21
 Riley, T. E., Watts, A. L., Ray, P. S., et al. 2021, *ApJL*, **918**, L27

Romani, R. W., Kandel, D., Filippenko, A. V., Brink, T. G., & Zheng, W. 2022, [ApJL](#), 934, L18

Ruiz, M., Shapiro, S. L., & Tsokaros, A. 2018, [PhRvD](#), 97, 021501

Shibata, M., Zhou, E., Kiuchi, K., & Fujibayashi, S. 2019, [PhRvD](#), 100, 023015

Tews, I., Carlson, J., Gandolfi, S., & Reddy, S. 2018, [ApJ](#), 860, 149

The LIGO Scientific Collaborationthe Virgo Collaboration, Abbott, B. P., et al. 2019, [PhRvX](#), 9, 011001

Tootle, S. D., Papenfort, L. J., Most, E. R., & Rezzolla, L. 2021, arXiv:2109.00940